第 51 卷第 9 期
2022 年 9 月

光　子　学　报
ACTA PHOTONICA SINICA

Vol.51 No.9
September 2022

引用格式：REN Qianyu, JIA Pinggang, QIAN Jiang, et al. Three-wavelength Dynamic Demodulation Technique for Multi-cavity Fiber Fabry-Perot Sensor[J]. Acta Photonica Sinica, 2022, 51(9):0906005
任乾钰,贾平岗,钱江,等. 多腔型光纤法布里-珀罗传感器三波长动态解调技术[J]. 光子学报,2022,51(9):0906005

多腔型光纤法布里-珀罗传感器三波长动态解调技术

任乾钰,贾平岗,钱江,王军,刘文怡,熊继军

（中北大学 省部共建动态测试技术国家重点实验室, 太原 030051）

摘　要：针对在多腔型法布里-珀罗传感器中难以提取动态信号的问题,提出了一种用于多腔型法布里-珀罗传感器的三波长解调技术。该解调技术使用放大自发辐射光源和三个固定中心波长的宽带光纤滤波器,使干涉现象仅发生在多腔型光纤法布里-珀罗传感器的短腔中,以此提取较短腔的三个干涉信号。建立了校正算法和反正切算法来提取振动信号。实验结果表明,该解调技术成功提取了频率为1 kHz、峰峰值幅度为2.6 μm的振动信号。解调速度为500 kHz,解调分辨率为0.25 nm。该解调技术具有系统紧凑、成本低、速度快、鲁棒性高等优点,在多腔型法布里-珀罗传感器方面有巨大的潜力。

关键词：法布里-珀罗腔;光纤传感器;三波长解调算法;低相干干涉;腔长解调

中图分类号：TP212.6　　**文献标识码**：A　　**doi**：10.3788/gzxb20225109.0906005

0　引言

光纤法布里-珀罗(Fabry - Pérot,F-P)传感器在航空航天、大型建筑、石油采集和许多其他领域具有广泛的应用[1-4]。在这些领域内,许多动态信号都需要被测量,例如动态压力、振动、声和超声。在超声测量中,动态信号的频率可以高达40 kHz[5]。为了测量这些参数,人们研究了各种光纤F-P传感器。随着光纤F-P传感器的发展,具有多个F-P腔的多腔型光纤F-P传感器由于具有某些优点成为了光纤F-P传感器的重要组成部分。在航空发动机测试领域,动态压力是经常需要测量的关键参数,而具有多个F-P腔的微机电系统(Micro-Electro-Mechanical System, MEMS)外腔式法布里-珀罗干涉仪(Extrinsic Fabry-Pérot Interferometer,EFPI)压力传感器由于其一致性和气密性,通常被设计用于航空发动机压力测量[6-9]。此外,多腔型光纤F-P传感器还常被用于多参数测量[10-12]。采用不同长度的不同F-P腔测量不同的参数,就能够实现多参数测量。因此,多腔型F-P传感器在工程应用中变得越来越重要。然而,多腔型F-P传感器中的动态信号仍然难以提取。

目前可用于多腔型F-P传感器的解调方法包括傅里叶变换解调法、互相关解调法和非扫描式互相关解调法。傅里叶变换解调法通过从光谱数据中提取频率或相位信息来解调F-P传感器[13-14]。互相关解调法是使用光谱数据进行互相关运算以找到互相关结果的峰值位置以解调F-P传感器的腔长[15]。这两种使用光谱仪的解调方法是常见的解调方式,但两种方法的解调速度都受到光谱仪采样率的限制。非扫描式互相关解调法使用电荷耦合器件,找到两个干涉仪之间的光程差(Optical Path Difference,OPD)相等的峰值位置,利用峰值位置获取腔长,但其解调速度仍然难以超过3 kHz[16-17]。

为了在多腔型F-P传感器中提取动态信号,本课题组先前提出了一种双波长解调技术,使干涉现象只发生在短腔内[18]。虽然双波长解调技术系统更简单,但双波长解调法容易受到光纤损耗的影响[18-22]。相比

基金项目：国家自然科学基金(Nos. 51935011, 52075505),国家自然科学基金创新研究群体项目(No. 51821003),国家重大科技专项(No. J2019-V-0015-0110)

第一作者：任乾钰(1992—),男,博士研究生,主要研究方向为光纤传感技术。Email: B1806005@st.nuc.edu.cn.com
导师(通讯作者)：熊继军(1971—),男,教授,博士,主要研究方向为动态测试技术、微纳传感器件与系统。Email: xiongjijun@nuc.edu.cn

收稿日期：2022-02-18;**录用日期**：2022-04-06

起双波长解调技术，三波长解调技术对于光纤的扰动所引起的损耗更加不敏感[23]。1999年，SCHMIDT M等[21]提出了一种基于超发光二极管光源的三波长正交相位解调方法。2019年，LIU Qiang等[22]提出了一种基于MG-Y激光器的三波长正交相位解调技术，消除了光路的不平衡。但是，三波长正交相位解调技术必须与腔长相匹配。2019年，JIA Jingshan等[23]提出了一种可用于任意腔长的基于三个激光器的EFPI传感器三波长解调技术。

本文提出了一种基于宽带光源的改进型的三波长相位解调技术，用于多腔型F-P传感器中的最短腔的动态解调。使用平顶型放大自发辐射（Amplified Spontaneous Emission，ASE）光源和三个宽带光纤滤波器来确保干涉现象仅发生在短腔中，利用改进型的三波长解调算法和三路光信号获取两路正交信号，使用反正切算法，利用正交信号提取振动信号。通过引入第三路光信号，消除了光纤扰动造成的影响。与以往的三波长相位校准算法相比，所提出的相位校准算法更加简洁。本文提出的三波长动态解调技术可以在很大程度上拓宽多腔型F-P传感器的应用。

1 解调算法与解调原理

1.1 多腔型光纤F-P传感器工作原理

多腔型光纤F-P传感器的典型结构如图1。多腔型光纤F-P传感器往往具有三个或三个以上的反射面，并且各个反射面之间的间距各不相同，以此来区分不同F-P腔的信号。当任意的F-P腔腔长受外界被测参数影响而发生变化时，就可以通过F-P腔腔长的变化情况对外界参数进行测量。

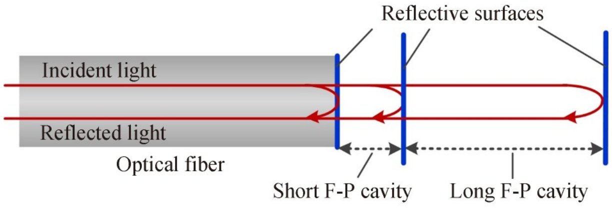

图1 多腔型光纤EFPI传感器的典型结构
Fig. 1 Structure of typical multi-cavity fiber-optic EFPI sensor

1.2 低相干干涉原理

低相干干涉又称白光干涉，是指具有一定带宽的光信号所产生的干涉现象，其所产生的干涉现象是带宽范围内所有波长的干涉光强度的总和。具有一定带宽的光信号仅能在有限长的相干长度范围内才能出现干涉现象。

相干长度定义为

$$C=\frac{\lambda_c^2}{\Delta\lambda} \tag{1}$$

式中，C是相干长度，λ_c是光电探测器接收到的光信号的中心波长，$\Delta\lambda$是光信号的带宽。当F-P腔引入的光程差小于光电探测器接收到的光的相干长度时，就会发生干涉。相反，当F-P腔引入的光程差逐渐增大时，干涉现象逐渐变得不明显。当F-P传感器引入的光程差远大于相干长度时，可以认为干涉消失了。利用低相干干涉原理，可以使干涉现象仅发生在多腔型光纤F-P传感器的短腔中，避免长腔对信号解调的影响，从而提取使用短腔测量的外界参数变化情况。

1.3 三波长解调算法与解调原理

根据低相干干涉原理，搭建了如图2所示的解调系统，用于多腔型F-P传感器中短腔的动态信号解调。光源使用的是波长范围为1 525～1 600 nm的平顶型ASE光源。ASE光源的功率为20 mW。多腔型EFPI传感器由渐变折射率（Graded Index，GRIN）透镜和固定在压电换能器（Piezoelectric Transducer，PZT）上的300 μm厚的双面抛光石英玻璃组成。石英玻璃的反射率约为0.04，GRIN透镜的反射率约为0.05。耦合器将光束分成三路，并通过三个中心波长分别为1 548.14 nm、1 550.224 nm和1 552.744 nm的光纤光栅滤波器。三个滤波器的3 dB带宽均为15 nm。使用三个光电探测器（Photodiode，PD）获得每个中心波长的三个

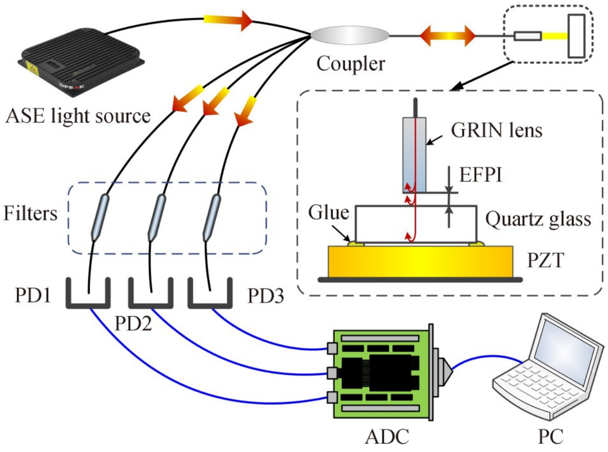

图2　应用于多腔型F-P传感器的三波长解调技术示意

Fig. 2　Schematic of the three-wavelength demodulation technology for the interrogation of multi-cavity F-P sensors

干涉信号。电压信号通过模数转换模块（Analog-to-Digital Converter，ADC）收集并传输到个人计算机（Personal Computer，PC）。ADC模块的输入电压范围为0～10 V，分辨率为12位，采样率500 kHz。光电探测器接收到的光的相干长度分别为159.882 μm、160.21 μm和160.73 μm。在该解调技术中，短F-P腔的长度需要小于相干长度的一半，大约80 μm以内；而长F-P腔的长度应该远大于相干长度。本次试验中，石英玻璃引入的光程差约为864 μm，远大于相干长度，因此在石英玻璃片的上下表面之间的干涉现象非常不明显，可以被忽略。

低精细度的EFPI传感器可以近似为双光束干涉仪。当光电探测器接收到的光信号为具有一定带宽的光信号时，传统的双光束干涉公式将无法使用，此时将使用低相干干涉公式。对于低精细度的EFPI传感器，不考虑传输过程中的损耗，光电探测器接收到的光强度为

$$\begin{aligned}I=&\int_{k_0-\frac{\Delta k}{2}}^{k_0+\frac{\Delta k}{2}}2I_0[1-\cos(4kn_1L_{\text{short}})]\mathrm{d}k+\int_{k_0-\frac{\Delta k}{2}}^{k_0+\frac{\Delta k}{2}}2I_0[1-\cos(4kn_2L_{\text{long}})]\mathrm{d}k+\\&\int_{k_0-\frac{\Delta k}{2}}^{k_0+\frac{\Delta k}{2}}2I_0\left[1-\cos(4kn_1L_{\text{short}}+n_2L_{\text{long}})\right]\mathrm{d}k=2I_0\Delta k\left[1-\frac{\sin(\Delta kn_1L_{\text{short}})}{\Delta kn_1L_{\text{short}}}\cos(2k_0n_1L_{\text{short}})\right]+\\&2I_0\Delta k\left[1-\frac{\sin(\Delta kn_2L_{\text{long}})}{\Delta kn_2L_{\text{long}}}\cos(2k_0n_2L_{\text{long}})\right]+\\&2I_0\Delta k\left[1-\frac{\sin(\Delta kn_1L_{\text{short}}+\Delta kn_2L_{\text{long}})}{\Delta kn_1L_{\text{short}}+\Delta kn_2L_{\text{long}}}\cos(2k_0n_1L_{\text{short}}+2k_0n_2L_{\text{long}})\right]\end{aligned}\tag{2}$$

式中，I是光电探测器接收到的光强度，I_0是光信号带宽内的初始光强度，$k=2\pi/\lambda$是波数，$\Delta k=2\pi/C$是波数域中的带宽，$k_0=2\pi/\lambda_c$是中心波长对应的波数，n_1和n_2分别是短腔和长腔的折射率，L_{short}和L_{long}分别是短空腔和长空腔的空腔长度。

当相干长度C大于$2n_1L_{\text{short}}$且远小于$2n_2L_{\text{long}}$时，干涉现象将会只发生在短F-P腔中。此时，光电探测器接收到的光信号可以近似为

$$I=6I_0\Delta k-2I_0\Delta k\frac{\sin(\Delta kn_1L_{\text{short}})}{\Delta kn_1L_{\text{short}}}\cos(2k_0n_1L_{\text{short}})\tag{3}$$

式中，$6I_0\Delta k$是与光学系统相关的直流分量。此时，光电探测器接收到的光强度变化将仅与短腔的腔长变化相关。

如图3所示，式(3)用于仿真三路光强信号。三路光信号的中心波长分别为1 548.14 nm、1 550.224 nm和1 552.744 nm，带宽均为15 nm。此时，光电探测器接收到的光的相干长度分别为159.882 μm、160.209 μm和160.73 μm。在较小的F-P腔长度范围内，例如40～50 μm，式(3)可以近似为

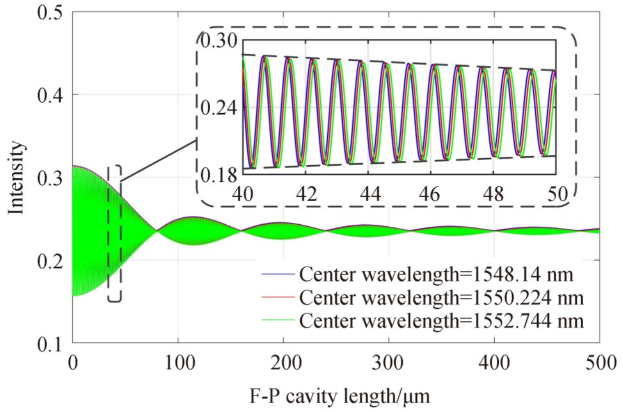

图3　中心波长分别为1 548.14 nm、1 550.224 nm和1 552.744 nm的干涉信号仿真图

Fig. 3　Diagram of interference signals simulation with the center wavelength of 1 548.14, 1 550.224, and 1 552.744 nm, respectively

$$I = A + B(L)\cos(2k_0 n_1 L_{\text{short}}) \tag{4}$$

式中，$A = 6I_0\Delta k$为直流项，$B(L) = -2I_0\Delta k\dfrac{\sin(\Delta k n_1 L_{\text{short}})}{\Delta k n_1 L_{\text{short}}}$为干涉项的振幅函数。在腔长变化较小的范围内，$B(L)$可被视为线性函数。当三路光信号的$\Delta k$值接近且初始光功率$I_0$相同时，三路光信号的$A$和$B(L)$可以认为近似相等。此时，三个光电探测器接收的光强度可近似为

$$I_1 = A + B(L)\cos(\theta_1) \tag{5}$$

$$I_2 = A + B(L)\cos(\theta_2) \tag{6}$$

$$I_3 = A + B(L)\cos(\theta_3) \tag{7}$$

式中，I_1、I_2和I_3分别为三个光电探测器接收的光强信号，$\theta_1 = 4\pi n_1 L_0/\lambda_1$、$\theta_2 = 4\pi n_1 L_0/\lambda_2$和$\theta_3 = 4\pi n_1 L_0/\lambda_3$分别是由三个光电探测器接收的光信号的初始相位，$\lambda_1$、$\lambda_2$和$\lambda_3$($\lambda_1 < \lambda_2 < \lambda_3$)分别是三个光信号的中心波长。$L_0$是短F-P腔的初始长度。当短腔长度开始改变时，光电探测器接收到的光强信号变为

$$I_1 = A + B(L)\cos(\theta_1 + \Delta\theta_1) \tag{8}$$

$$I_2 = A + B(L)\cos(\theta_2 + \Delta\theta_2) \tag{9}$$

$$I_3 = A + B(L)\cos(\theta_3 + \Delta\theta_3) \tag{10}$$

式中，$\Delta\theta_1 = 4\pi n_1\Delta L/\lambda_1$、$\Delta\theta_2 = 4\pi n_1\Delta L/\lambda_2$和$\Delta\theta_3 = 4\pi n_1\Delta L/\lambda_3$是由短F-P腔腔长变化引起的相位变化，$\Delta L$是短F-P腔的腔长变化量。当$\Delta L \ll L_0$且$\lambda_1 \approx \lambda_2 \approx \lambda_3$时，$\Delta\theta_1$、$\Delta\theta_2$和$\Delta\theta_3$可被认为近似相等。因此，式(8)～(10)可近似为

$$I_1 = A + B(L)\cos(\theta_1)\cos(\Delta\theta) - B(L)\sin(\theta_1)\sin(\Delta\theta) \tag{11}$$

$$I_2 = A + B(L)\cos(\theta_2)\cos(\Delta\theta) - B(L)\sin(\theta_2)\sin(\Delta\theta) \tag{12}$$

$$I_3 = A + B(L)\cos(\theta_3)\cos(\Delta\theta) - B(L)\sin(\theta_3)\sin(\Delta\theta) \tag{13}$$

当短腔的初始腔长能够通过静态解调技术提前获取时，θ_1、θ_2和θ_3也能够通过$\theta_1 = 4\pi n_1 L_0/\lambda_1$、$\theta_2 = 4\pi n_1 L_0/\lambda_2$和$\theta_3 = 4\pi n_1 L_0/\lambda_3$提前获取。相位变化量的两路正交信号可以表示为

$$F_1 = B(L)\sin(\Delta\theta) = \frac{(I_1 - I_2)(\cos\theta_2 - \cos\theta_3) - (I_2 - I_3)(\cos\theta_1 - \cos\theta_2)}{(\cos\theta_1 - \cos\theta_2)(\sin\theta_2 - \sin\theta_3) - (\cos\theta_2 - \cos\theta_3)(\sin\theta_1 - \sin\theta_2)} \tag{14}$$

$$F_2 = B(L)\cos(\Delta\theta) = \frac{(I_1 - I_2)(\sin\theta_2 - \sin\theta_3) - (I_2 - I_3)(\sin\theta_1 - \sin\theta_2)}{(\cos\theta_1 - \cos\theta_2)(\sin\theta_2 - \sin\theta_3) - (\cos\theta_2 - \cos\theta_3)(\sin\theta_1 - \sin\theta_2)} \tag{15}$$

式(14)和式(15)中的F_1和F_2此时就成为了两路正交信号。此时，相位变化量$\Delta\theta$就可以使用反正切算法获得

$$\Delta\theta' = \arctan\left(\frac{F_1}{F_2}\right) \tag{16}$$

由于反正切函数的值域范围为$-\pi/2$到$\pi/2$，此时如果相位变化量$\Delta\theta$超出这个范围，那么利用反正切法

提取的相位$\Delta\theta'$将会无法准确反映$\Delta\theta$。但如果$\Delta\theta'$在连续变化的情况下，只要有足够高的采样率，那么就会在相位$\Delta\theta$变化的过程中，$\Delta\theta'$出现从$-\pi/2$到$\pi/2$的跳变点，或从$\pi/2$到$-\pi/2$的跳变点。通过对跳变点的判断，就可以利用相位补偿技术，获取准确的相位$\Delta\theta$。此时相位变化量可以表示为

$$\Delta\theta=\Delta\theta'\pm m\pi \tag{17}$$

式中，m代表非负整数。之后，通过第一路光的相位变化，就可以求得传感器的腔长变化，即

$$\Delta L=\frac{\lambda_2}{4\pi}\Delta\theta \tag{18}$$

通过引入第三路光信号，干涉信号的直流分量通过三路光信号之间的减法运算相互抵消，这使得光传输过程中的损耗无法对解调结果造成影响。并且，根据式(14)和式(15)可以看出，本文所述的三波长解调技术，能够对相干长度内任意腔长的EFPI传感器进行解调，并且还在双波长解调技术的基础上消除了光功率变化的影响，提高了解调系统的鲁棒性，使得该解调技术能够广泛适用于工程应用环境。

2 解调算法仿真分析

为了验证三波长解调算法的可行性，利用三波长解调算法公式进行仿真分析。传感器的初始腔长L_0设置为45 μm，折射率设置为1。三路光信号的中心波长分别设置为1 548.14 nm、1 550.224 nm和1 552.744 nm，带宽都设置为15 nm。传感器的腔长以正弦变化，腔长变化范围为±1.5 μm。光强信号利用式(3)进行仿真，仿真结果如图4。

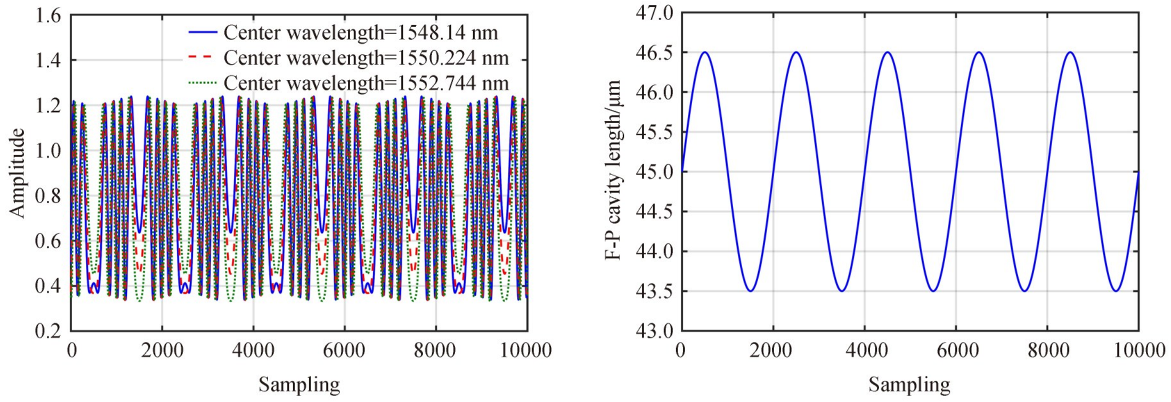

(a) Interference signals I_1, I_2 and I_3　　(b) Waveform of demodulation results

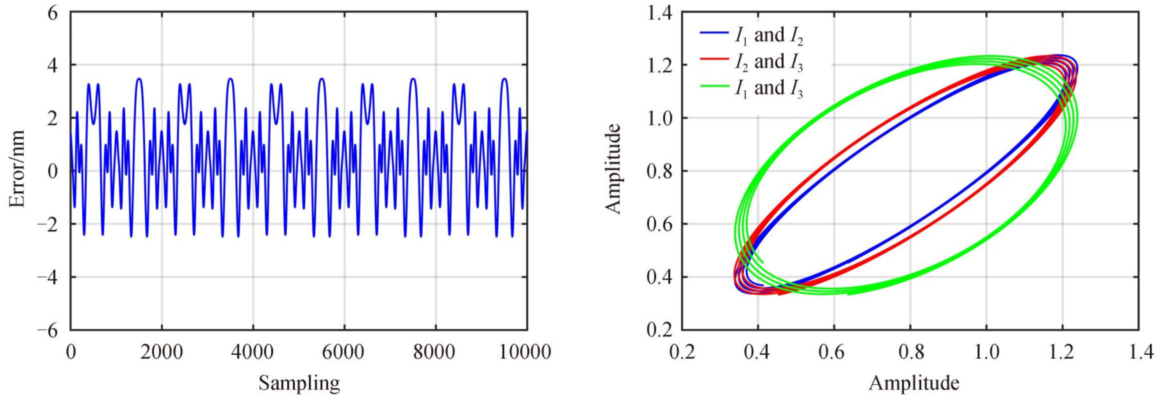

(c) Error of demodulation results　　(d) The Lissajous figures for I_1, I_2 and I_3

图4　解调算法仿真结果

Fig. 4　The simulation results of the demodulation algorithm

三波长解调算法仿真结果如图4。由频率为250 Hz的正弦信号驱动的三路光强信号如图4(a)，解调结果如图4(b)。如图4(b)所示，三波长解调算法成功提取出了正弦信号。解调误差如图4(c)。在±1.5 μm范围内，解调误差小于4 nm。但随着腔长的增加，解调误差会逐渐增大。当腔长变化超过±5 μm时，最大解调

误差将达到10 nm。在实际的解调系统中，由于噪声的影响，解调误差会超过10 nm。因此，为了获得准确的解调结果，腔长变化应在±5 μm以内。如图4(d)所示，三波长解调算法中的三路光信号采用李萨如图进行评估，尽管三个光信号之间的相位差不具有正交关系，但利用三波长解调算法，依然能够得到校正后正交信号并提取相位变化量。仿真结果表明应用于多腔型光纤F-P传感器的三波长解调技术具有可行性。

3 解调算法实验研究

为了评估三波长解调技术的可行性，使用如图2所示的实验系统进行实验，使用PZT驱动1 kHz的振动信号测试了多腔型EFPI传感器三波长解调技术。PZT的峰-峰值幅度约为2.6 μm。初始腔长为39.29 μm。F-P腔的初始腔长通过WLI技术[13]和高次谐波互相关算法[15]解调获得。在获得初始腔长参数后，与初始腔长有关的参数$\sin\theta_1$, $\sin\theta_2$, $\sin\theta_3$, $\cos\theta_1$, $\cos\theta_2$和$\cos\theta_3$被解调系统计算获得。当PZT开始振动时，ADC采集三个信号并解调，解调速度为500 kHz。

为了研究解调系统的噪声性能，在实验前，选取了一段解调结果对解调系统的噪声进行测量，如图5。系统的分辨率通过这段解调结果的标准差进行分析，标准差为0.25 nm。因此，本文所述的三波长解调系统的分辨率为0.25 nm。

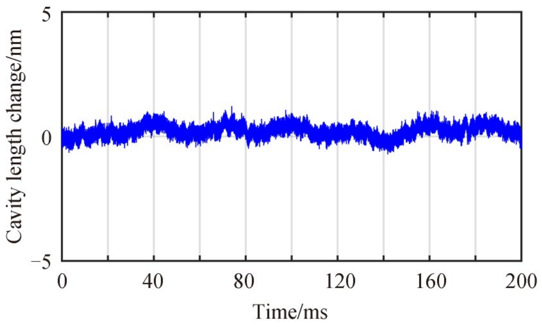

图5 解调系统噪声性能

Fig. 5 The noise performance of the demodulation system

光电探测器接收到的三路电压信号如图6(a)，解调结果如图6(b)。解调得到的振动信号峰峰值为2.59 μm。得到三个电压信号后，首先对由于光源平坦度、光电探测器增益不同、光纤滤波器透射率不同而引起的光功率不平衡进行校准。在本次实验中，I_2和I_3分别放大了1.2倍和1.45倍。通过对比图4和图6，可以看出实验结果成功地验证了仿真结果。实验结果表明，利用三波长解调技术成功解调了PZT驱动的振动信号。图6(c)为李萨如图，三波长解调技术可以利用三个光信号之间的任意相位差进行解调。比较图4(d)和图6(c)，实验中的得到的李萨如图与仿真得到的李萨如图在趋势上基本保持一致。功率密度谱如图6(d)所示。可以看出，三波长解调技术从三路光信号中提取出了1 kHz的振动信号。实验结果表明，三波长解调技术成功的在多腔型EFPI传感器中提取出了短腔中的正弦振动信号，证明了该解调技术具有可行性。

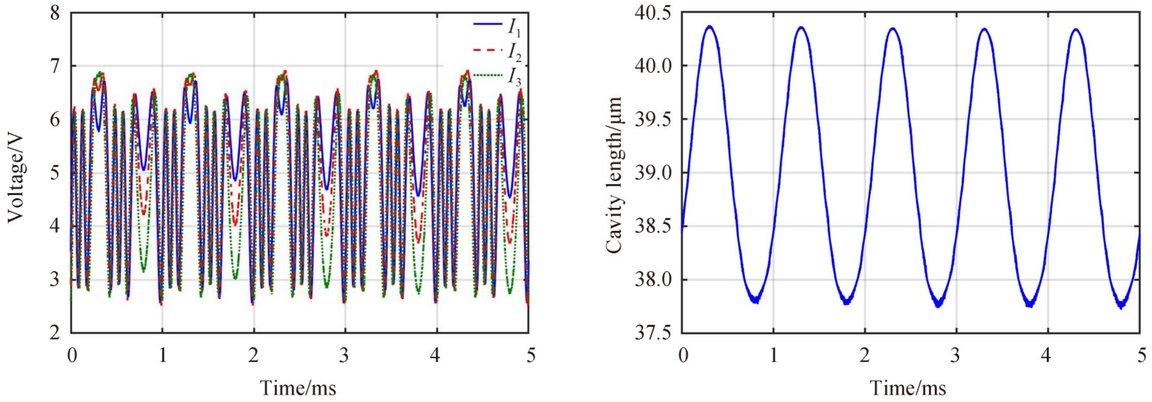

(a) I_1, I_2 and I_3 was driven by a 1 kHz sinusoidal signal

(b) Waveform of demodulation results

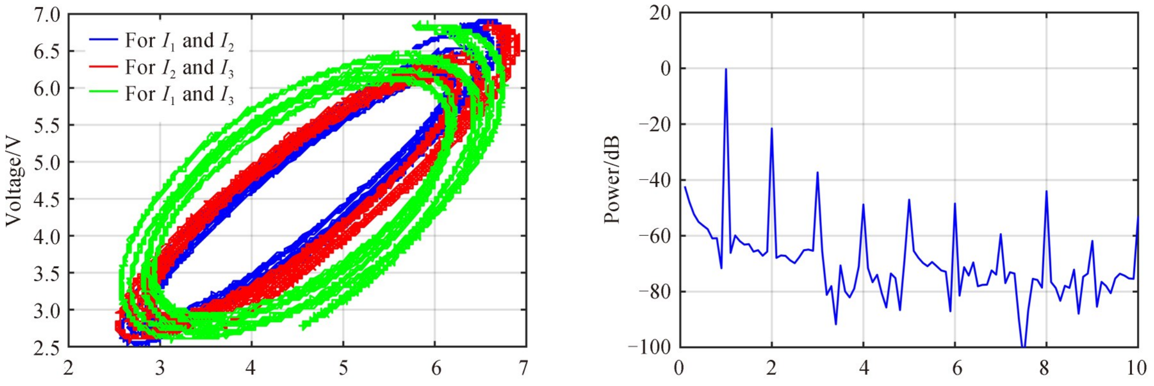

(c) The Lissajous figures for I_1, I_2 and I_3　　(d) Power spectrum plots of the demodulation signal

图6　F-P 腔初始腔长为 39.29 μm 的实验结果

Fig. 6　The experimental results with initial F-P cavity length of 39.29 μm

为了验证该解调技术能够应用于任意腔长的F-P传感器,将短F-P腔的腔长调整为64.8 μm,之后重新进行上述实验。PZT的参数设置与上述实验均保持一致。实验结果如图7,光电探测器接收到的三个电压信号如图7(a),解调结果如图7(b)。解调技术提取的振动信号峰峰值为2.62 μm。实验结果证明,该解调技术可以提取相关长度内的任意初始短腔长度的多腔型F-P传感器中的动态信号。

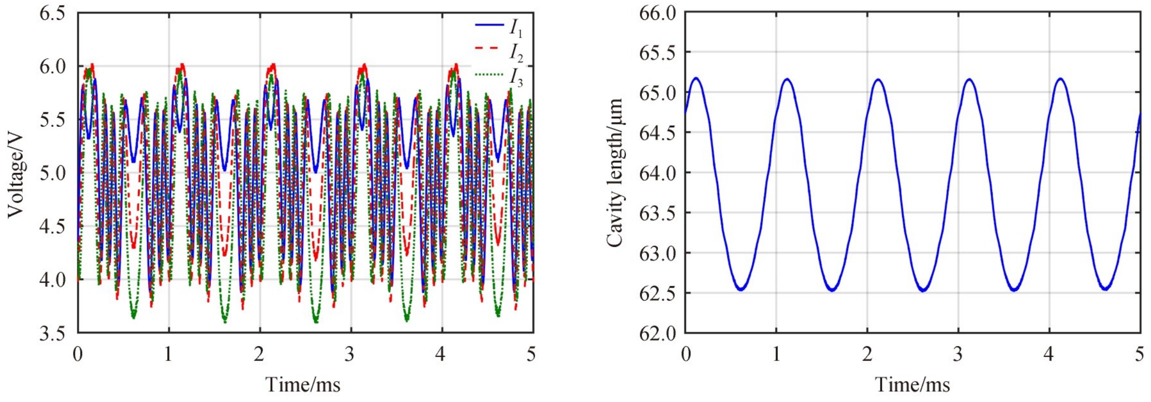

(a) I_1, I_2 and I_3 was driven by a 1 kHz sinusoidal signal　　(b) Waveform of demodulation results

图7　F-P 腔初始腔长为 64.8 μm 的实验结果

Fig. 7　The experimental results with initial F-P cavity length of 64.8 μm

4　结论

本文提出了一种可用于多腔型F-P传感器动态信号解调的三波长解调技术。利用该解调技术成功在多腔型F-P传感器的短腔中提取出了峰-峰值幅度为2.6 μm的1 kHz振动信号。本文所述的三波长解调技术通过使用平顶型ASE光源和三个宽带光纤滤波器,使得干涉现象只发生在较短的F-P腔中。通过改进型的三波长解调算法的公式可以看出,该解调算法可以用于相干长度内任意腔长的光纤F-P传感器。并且三波长解调技术通过数学运算消除了直流分量的干扰,从而使解调系统可以降低光纤扰动产生的噪声。本文所述的解调技术能够在多腔型F-P传感器中提取动态信号。虽然仅能够提取多腔型F-P传感器中较短腔的动态信号,但如果同时使用光谱仪,就可以同时提取短F-P腔测得的动态信号和长F-P腔测得的静态信号,这将大大拓宽多腔型光纤F-P传感器的应用范围。该系统具有系统紧凑、成本低、解调速度快、鲁棒性强等优点,在多腔型光纤F-P传感器的动态信号提取中具有广阔的应用前景。

参考文献

[1]　JIA Pinggang, FANG Guocheng, LIANG Ting, et al. Temperature-compensated fiber-optic Fabry-Perot interferometric gas refractive-index sensor based on hollow silica tube for high-temperature application[J]. Sensors and Actuators B:

Chemical, 2017, 244: 226-232.

[2] JIHAENG Y, LALLY E, WANG Anbo, et al. Demonstration of an all-sapphire Fabry-Pérot cavity for pressure sensing [J]. IEEE Photonics Technology Letters, 2011, 23(1): 9-11.

[3] WANG Jiajun, DONG Bo, LALLY E, et al. Multiplexed high temperature sensing with sapphire fiber air gap-based extrinsic Fabry-Perot interferometers[J]. Optics Letters, 2010, 35(5): 619-621.

[4] YANG Yang, WANG Mohan, YU Zhihao, et al. Multiplexable intrinsic Fabry-Pérot interferometers inscribed by femtosecond laser for vibration measurement in high temperature environments[J]. Sensors and Actuators A: Physical, 2021, 321:112562.

[5] JIANG Junfeng, ZHANG Tianhao, WANG Shuang, et al. Noncontact ultrasonic detection in low-pressure carbon dioxide medium using high sensitivity fiber-optic Fabry-Perot sensor system[J]. Journal of Lightwave Technology, 2017, 35(23): 5079-5085.

[6] MA Weiyi, JIANG Yi, HU Jie, et al. Microelectromechanical system-based, high-finesse, optical fiber Fabry-Perot interferometric pressure sensors[J]. Sensors and Actuators A: Physical, 2020, 302:111795.

[7] LIU Jia, JIA Pinggang, FENG Fei, et al. MgO single crystals MEMS-based fiber-optic Fabry-Perot pressure sensor for harsh monitoring[J]. IEEE Sensors Journal, 2021, 21(4): 4272-4279.

[8] WANG Xue, JIANG Junfeng, WANG Shuang, et al. All-silicon dual-cavity fiber-optic pressure sensor with ultralow pressure-temperature cross-sensitivity and wide working temperature range[J]. Photonics Research, 2021, 9(4): 521-529.

[9] SHAO Zhiqiang, WU Yalin, WANG Shuang, et al. All-sapphire-based fiber-optic pressure sensor for high-temperature applications based on wet etching[J]. Optics Express, 2021, 29(3): 4139-4146.

[10] PEVEC S, DONLAGIC D. Miniature fiber-optic sensor for simultaneous measurement of pressure and refractive index [J]. Optics Letters, 2014, 39(21): 6221-6224.

[11] WANG Xue, JIANG Junfeng, WANG Shuang, et al. High-accuracy hybrid fiber-optic Fabry-Pérot sensor based on MEMS for simultaneous gas refractive-index and temperature sensing[J]. Optics Express, 2019, 27(4): 4204-4215.

[12] GAO Hongchun, JIANG Yi, CUI Yang, et al. Dual-cavity Fabry-Perot interferometric sensors for the simultaneous measurement of high temperature and high pressure[J]. IEEE Sensors Journal, 2018, 18(24): 10028-10033.

[13] JIANG Yi. Fourier transform white-light interferometry for the measurement of fiber-optic extrinsic Fabry-Pérot interferometric sensors[J]. IEEE Photonics Technology Letters, 2008, 20(2): 75-77.

[14] YU Zhihao, WANG Anbo. Fast white light interferometry demodulation algorithm for low-finesse Fabry-Pérot sensors [J]. IEEE Photonics Technology Letters, 2015, 27(8): 817-820.

[15] CHEN Haibin, LIU Jie, ZHANG Xiongxing, et al. High-order harmonic-frequency cross-correlation algorithm for absolute cavity length interrogation of white-light fiber-optic Fabry-Perot sensors[J]. Journal of Lightwave Technology, 2020, 38(4): 953-960.

[16] WANG Shuang, ZHANG Jinshi, JIANG Junfeng, et al. Position-deviation-compensation demodulation method for multi-channel polarized low-coherence interferometry[J]. Optics Express, 2018, 26(13): 17407-17417.

[17] YU Zhihao, TIAN Zhipeng, WANG Anbo. Simple interrogator for optical fiber-based white light Fabry-Perot interferometers[J]. Optics Letters, 2017, 42(4): 727-730.

[18] REN Qianyu, JIA Pinggang, FANG Guocheng, et al. Dual-wavelength demodulation technique for interrogating a shortest cavity in multi-cavity fiber-optic Fabry-Pérot sensors[J]. Optics Express, 2021, 29(20): 32658-32669.

[19] JIA Jingshan, JIANG Yi, ZHANG Liuchao, et al. Dual-wavelength DC compensation technique for the demodulation of EFPI fiber sensors[J]. IEEE Photonics Technology Letters, 2018, 30(15): 1380-1383.

[20] LIU Qiang, JING Zhenguo, LI Ang, et al. Common-path dual-wavelength quadrature phase demodulation of EFPI sensors using a broadly tunable MG-Y laser[J]. Optics Express, 2019, 27(20): 27873-27881.

[21] SCHMIDT M, FÜRSTENAU N. Fiber-optic extrinsic Fabry-Perot interferometer sensors with three-wavelength digital phase demodulation[J]. Optics Letters, 1999, 24(9): 599-601.

[22] LIU Qiang, JING Zhenguo, LIU Yueying, et al. Quadrature phase-stabilized three-wavelength interrogation of a fiber-optic Fabry-Perot acoustic sensor[J]. Optics Letters, 2019, 44(22): 5402-5405.

[23] JIA Jingshan, JIANG Yi, GAO Hongchun, et al. Three-wavelength passive demodulation technique for the interrogation of EFPI sensors with arbitrary cavity length[J]. Optics Express, 2019, 27(6): 8890-8899.

Three-wavelength Dynamic Demodulation Technique for Multi-cavity Fiber Fabry-Perot Sensor

REN Qianyu, JIA Pinggang, QIAN Jiang, WANG Jun, LIU Wenyi, XIONG Jijun
（*State Key Laboratory of Dynamic Measurement Technology*, *North University of China*, *Taiyuan* 030051, *China*）

Abstract: Fiber-optic Fabry-Pérot sensors have a wide range of applications, including aerospace, large-scale construction, oil collection, and many other fields. In many cases, dynamic parameters, such as dynamic pressure, vibration, acoustics, and ultrasonics are required to be measured. In order to measure these parameters, a variety of fiber-optic Fabry-Pérot sensors are produced. In some fields, the multi-cavity fiber-optic Fabry-Pérot sensor is inevitable for some advantages. For example, in the field of aerospace engine testing, dynamic pressure is a key parameter that often needs to be measured, and the micro-electro-mechanical system external Fabry-Pérot interferometer pressure sensors with multiple Fabry-Pérot cavities are often designed for aerospace engine pressure measurement due to their consistency and airtightness. Moreover, multi-cavity Fabry-Pérot sensors are good candidates for multi-parameter measurements. The different Fabry-Pérot cavities with different lengths are used to measure different parameters to achieve multi-parameter measurement. Therefore, multi-cavity Fabry-Pérot sensors are becoming increasingly important in engineering applications. However, extracting dynamic signals in multi-cavity Fabry-Pérot sensors is a challenge. In this paper, an improved passive three-wavelength phase demodulation technology based on a broadband light source is proposed for dynamic interrogation of the shortest cavity in a multi-cavity Fabry-Pérot sensor. According to the principle of low coherence interference, when the optical path difference introduced by the Fabry-Pérot interferometer is less than the coherent length received by the photodetectors, interference occurs. In contrast, when the optical path difference introduced by the Fabry-Pérot interferometers is longer than five times the coherence length, the interference phenomenon becomes insignificant and it can be considered that the interference disappears. Therefore, a flat-top amplified spontaneous emission light source and three broadband fiber filters were used to ensure the interference only occurs in the short cavity. The quadrature signals are obtained by three filtered optical signals with arbitrary cavity length using an improved phase calibration algorithm. The established signal calibration algorithm allows the demodulation technology for arbitrary short cavity lengths and arbitrary central wavelength. The demodulation technology can work without the direct-current voltages, so the demodulation system can reduce the fiber-optic disturbance noise. The arctangent algorithm is established to extract vibration signals by the quadrature signals. Compared with the previous phase calibration algorithm, the phase calibration algorithm proposed in the paper is more concise. The experimental system was consisted of a reflective bracket, a light source, a multi-cavity Fabry-Pérot interferometer, a fiber-optic coupler, three fiber filters, three photodiodes, an analog-to-digital conversion and a personal computer. The light from the light source passed through the fiber-optic coupler to the multi-cavity Fabry-Pérot interferometer. A multi-cavity Fabry-Pérot interferometer consists of a gradient-index lens and a 300-μm-thick double-polished quartz glass fixed on a piezoelectric transducer. The light reflected from the interferometer passed through the coupler and through the filters to the photodiodes. Three interferometric signals at each center wavelength were obtained using three photodiodes. The voltage signals were collected by analog-to-digital conversion and transmitted to a personal computer. The feasibility of the demodulation algorithm was verified by simulations and experiments. The experimental results show that the vibration signals with a frequency of 1 kHz and peak-to-peak amplitude of 2.6 μm is successfully extracted with different Fabry-Pérot cavity length, which proves that the three-wavelength demodulation algorithm can be used for optical fiber multi-cavity Fabry-Pérot sensor with arbitrary short cavity length. The demodulation speed is 500 kHz and the demodulation resolution is 0.25 nm. The demodulation technology makes it possible to extract dynamic signals in a multi-cavity Fabry-Pérot sensor. If the spectrometer is used at the same time, the dynamic signal measured by the short cavity and the static signal measured by the long cavity can be interrogated at the same time. This demodulation technology has the advantages of a compact system, low cost, fast speed and high robustness, illustrating its bright potential for multi-cavity Fabry-Pérot sensors.

Key words：Fabry-Pérot cavity；Fiber optics sensor；Three-wavelength demodulation algorithm；Low coherence interference；Cavity length interrogation

OCIS Codes：060.2370；120.2230；060.2300；120.5050

Foundation item：National Natural Science Foundation of China（Nos. 51935011，52075505），the Innovative Research Group Project of National Science Foundation of China（No. 51821003），the National Major Science and Technology Project of China（No. J2019-V-0015-0110）